ORIGINAL ARTICLE

Nanocutting mechanism of 6H-SiC investigated by scanning electron microscope online observation and stress-assisted and ion implant-assisted approaches

Zongwei Xu[1] · Lei Liu[1] · Zhongdu He[1] · Dongyu Tian[1] · Alexander Hartmaier[2] · Junjie Zhang[3] · Xichun Luo[4] · Mathias Rommel[5] · Kai Nordlund[6] · Guoxiong Zhang[1] · Fengzhou Fang[1]

Abstract
Nanocutting mechanism of single crystal 6H-SiC is investigated through a novel scanning electron microscope setup in this paper. Various undeformed chip thicknesses on (0001) < 1–100 > orientation are adopted in the nanocutting experiments. Phase transformation and dislocation activities involved in the 6H-SiC nanocutting process are also characterized and analyzed. Two methods of stress-assisted and ion implant-assisted nanocutting are studied to improve 6H-SiC ductile machining ability. Results show that stress-assisted method can effectively decrease the hydrostatic stress and help to activate dislocation motion and ductile machining; ion implant-induced damages are helpful to improve the ductile machining ability from MD simulation and continuous nanocutting experiments under the online observation platform.

Keywords Diamond turning · Silicon carbide · Phase transformation · Surface integrity · MD simulation · Ion beam machining

Abbreviations
|	
SiC	silicon carbide
SEM	scanning electron microscope
EBSD	electron backscatter diffraction
FIB	focused ion beam
ABOP	analytical bond order potential
DXA	dislocation extraction algorithm
SRIM	Stopping and Range of Ions in Matter
MD	molecular dynamics

✉ Zongwei Xu
zongweixu@tju.edu.cn

1   State Key Laboratory of Precision Measuring Technology & Instruments, Centre of MicroNano Manufacturing Technology, Tianjin University, Tianjin, China

2   Interdisciplinary Centre for Advanced Materials Simulation (ICAMS), Ruhr-University Bochum, Bochum, Germany

3   Center for Precision Engineering, Harbin Institute of Technology, Harbin, China

4   Centre for Precision Manufacturing, Department of Design, Manufacture & Engineering Management, University of Strathclyde, Glasgow, UK

5   Fraunhofer Institute for Integrated Systems and Device Technology (IISB), Erlangen, Germany

6   Department of Physics, Helsinki Institute of Physics POB 43, University of Helsinki, Helsinki, Finland

1 Introduction

Silicon carbide (SiC) has attracted considerable attention because of its outstanding properties, such as excellent chemical stability, a wide band gap, high thermal conductivity, and a high melting point. SiC-based devices are capable of working in harsh temperature, wear, chemical, and radiated environment [1]. Recently, SiC had showed self-healing on fractured amorphous and crystalline surfaces, which provides new insights to design and fabricate high performance devices, working in harsh environments to avoid catastrophic failures [2, 3]. However, the properties of brittleness and high hardness of SiC [4] make it difficult to be used for fabricating ultra-precision micro-/ nano-components, such as producing miniaturized functional surfaces. Damages such as surface micro-crack and subsurface damage often occur during machining of SiC [5]. Besides, at ambient condition, SiC can form

Fig. 1 Experimental setup of the nanometric cutting: **a** setup inside the vacuum chamber of SEM/FIB, **b** morphology of the diamond cutting tool
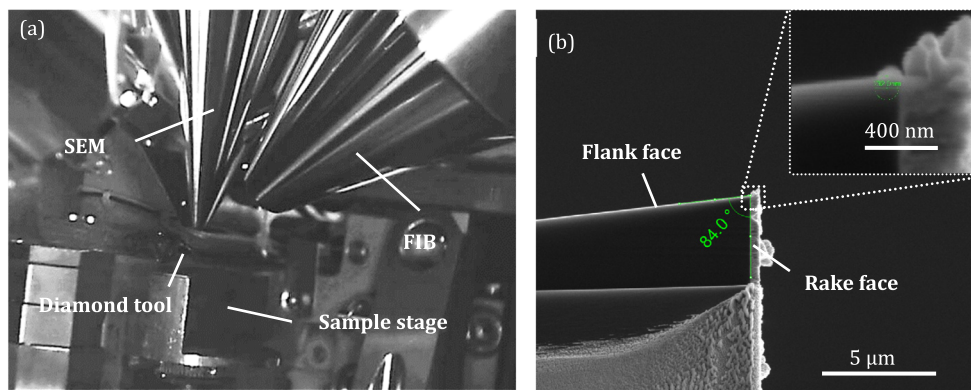
many different polytypes that originate from differences in the stacking sequence of the silicon-carbon bilayers along [111] or [0001] direction [6]. About 200 polytypes of SiC are found at atmospheric pressure [7]. Single crystal 6H-SiC for being one of the commercially available polytypes and of high interest for optoelectronic applications is adopted in this study.

On the other hand, the surface integrity is of great importance for the semiconductor devices. Studies have shown that hard and brittle materials can also achieve ductile removal. So many scholars are devoted to study the ductile regime machining of brittle materials. Studies have shown that when the ratio of the undeformed chip thickness to the tool edge radius is less than a critical value, the chip formation occurs via extrusion [8–12]. A novel model of maximum undeformed chip thickness for

face grinding is proposed, which is in good agreement with the experimental results on hard- and soft-brittle materials [13–15]. A novel approach of single grain scratching is performed at ~m/s speed at nanoscale depth of cut, which is three to six orders magnitude higher than the traditional nanoscratching [16–18]. This approach opens a new route to investigate the fundamental mechanisms of abrasive machining on brittle materials. Mechanical chemical machining is developed recently for brittle materials [19, 20]. As a typical semiconductor material, the mechanism of the ductile regime machining of single crystal 6H-SiC has attracted the attention of many researchers. Patten et al. [21] performed single point diamond turning experiments on single crystal 6H-SiC. They pointed out that the ductile chips were amorphous and inferred that the ductility of 6H-SiC during machining
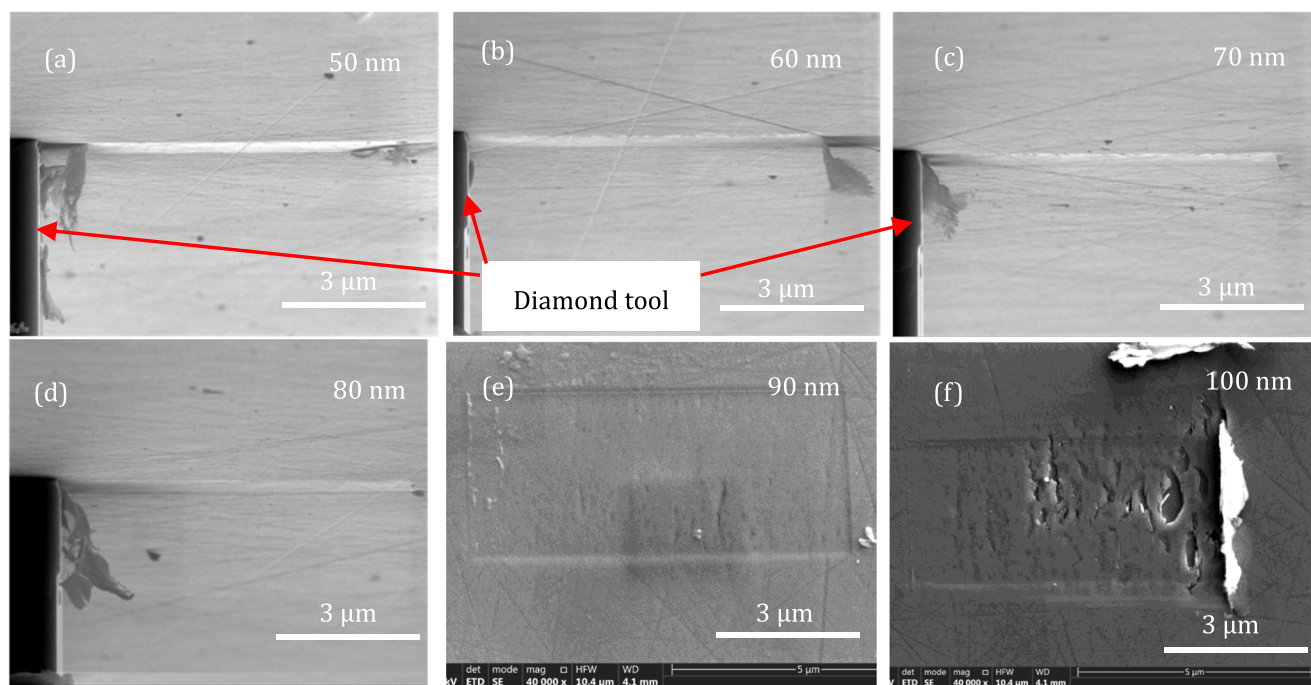

Fig. 2 SEM photographs of nanocutting surface morphology for different undeformed chip thicknesses
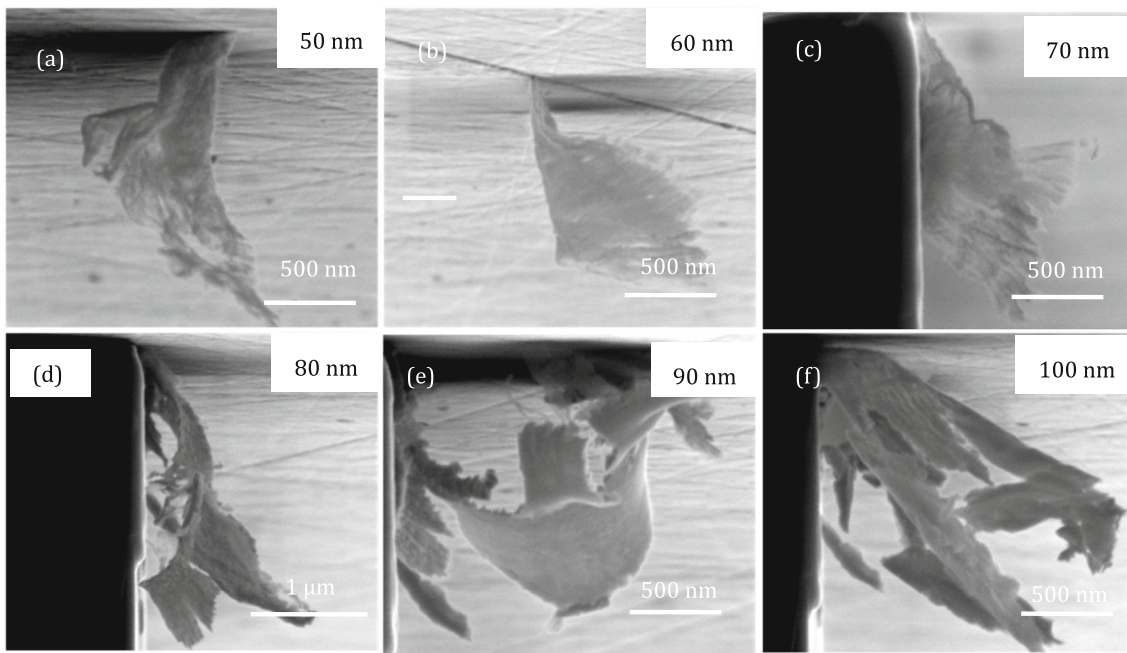
Fig. 3 SEM photographs of nanocutting chip morphology for different undeformed chip thicknesses

was due to the formation of a high-pressure phase. Wu et al. [22] conducted nanocutting simulations of single crystal 6H-SiC through molecular dynamics (MD) technique. The dislocation and structural analysis revealed that the plastic deformation of 6H-SiC could be realized

by either phase transformation from the Wurtzite structure to an amorphous structure or by the migration of dislocations on the basal plane or pyramidal plane, as well as by a combination of them. Nanoscratching tests were conducted on the surface of 6H-SiC (0001) using Berkovich
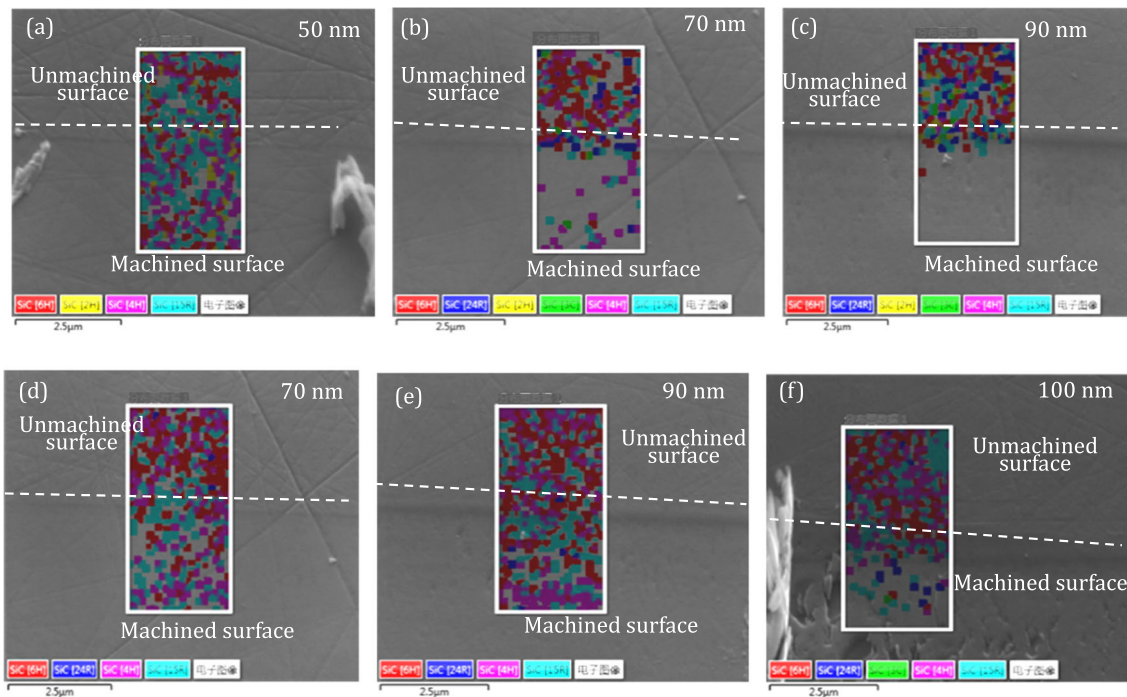

Fig. 4 EBSD images of phase identification and distribution of 6H-SiC after nanocutting. **a, b, c** are EBSD results under 15 kV and 2.2 nA for undeformed chip thicknesses of 50 nm, 70 nm, and 90 nm, respectively. **d, e, f** are the EBSD results under 20 kV and 2.4 nA for undeformed chip thicknesses of 70 nm, 90 nm, and 100 nm, respectively. The white dashed lines indicate the boundary between nanocutting area and non-machining area
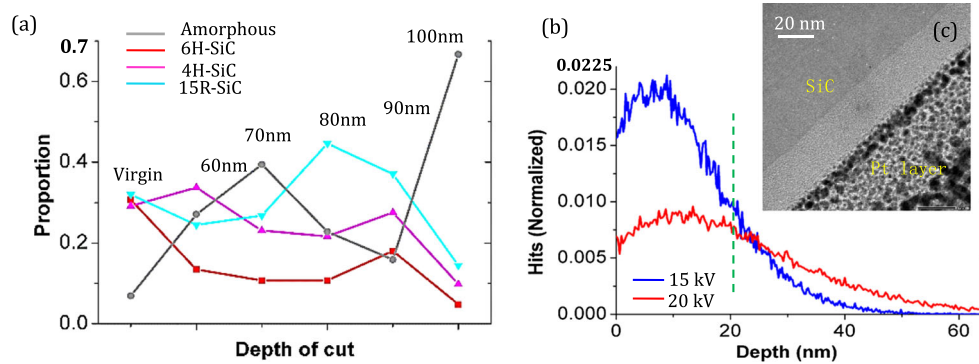
Fig. 5 **a** Proportion of SiC crystal structure changed with different depths of cut based on the EBSD (20 kV, 2.4 nA) data. **b** Penetration depth of the backscattered electrons with 15 kV and 20 kV (Casino simulation: SiC substrate, with minimum electron energy of 14.25 keV and 19 keV, respectively, and number of simulated electrons = 10^6). **c** TEM result of machined 6H-SiC with 90 nm depth of cut

nanoindenter by Meng et al. [23]. With transmission electron microscopy being used for phase and dislocation analysis, they confirmed that the plastic deformation mechanism of 6H-SiC during the ductile regime machining was most likely a combination of dislocation activities and high-pressure phase transformation. Zhang et al. [24] performed nanoscratching tests on single crystal 6H-SiC, and they concluded that the elastic recovery of the material, the geometry of the tip, and the stress distribution of the interface between the tip and sample had large influences on the machined depth. Indentation experiments were conducted on the surface of 6H-SiC by Li et al. [25]. And they revealed that the existence dislocations in the subsurface should be occurred earlier than cleavage. These dislocations were the predominant yielding mechanism in 6H-SiC. Goel et al. [26] performed diamond turning of single crystal 6H-SiC and revealed that phase transformation should be considered as a prerequisite to ductile regime machining. Xiao et al. [27] conducted MD simulations and taper cutting to investigate the atomic details of ductile deformation in the machining of single crystal 6H-SiC. The results indicated that the origin of ductile response for 6H-SiC was a combination of high-pressure phase transformation (HPPT) to rock salt structure and dislocation activities, while dislocation plasticity played a major role. They further studied the effect of the tool rake angle on the chip formation. It was found that the mechanism of chip formation transformed from shearing to extrusion when the tool rake angle varied from 0° to −40° [28]. Luo et al. studied atomistic aspects of ductile responses of SiC during nanometric cutting; it was considered that 3C-SiC undergone sp3-sp2 order-disorder transition resulting in the formation of SiC-graphene-like which caused ductile response [29].

The above studies have greatly enriched researchers' understanding on the mechanism of ductile removal regime machining of single crystal 6H-SiC. However, controversy still exists regarding the basic mechanism of ductile deformation in the ductile regime machining of 6H-SiC. Some novel methods are developed recently for brittle materials so as to effectively improve the nanomachining ability of hard and brittle materials, such as mechanical chemical polishing [30] and ion implant-assisted [31] and stress-assisted machining [32].

The ductile removal mechanism of single crystal 6H-SiC is studied in this paper. The nanometric cutting experiments for different undeformed chip thicknesses were carried out on a novel nanometric cutting setup within a scanning electron microscope (SEM). Characterization of the machined surface was carried out by using electron backscatter diffraction (EBSD) and Raman spectroscopy. By combining the MD simulation and continuous nanocutting experiments under the online observation platform, both stress-assisted and ion-implant-assisted nanocutting experiments are studied to improve 6H-SiC ductile machining ability.
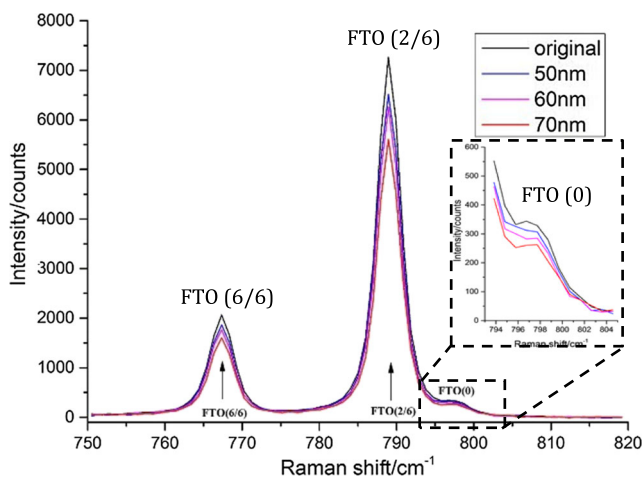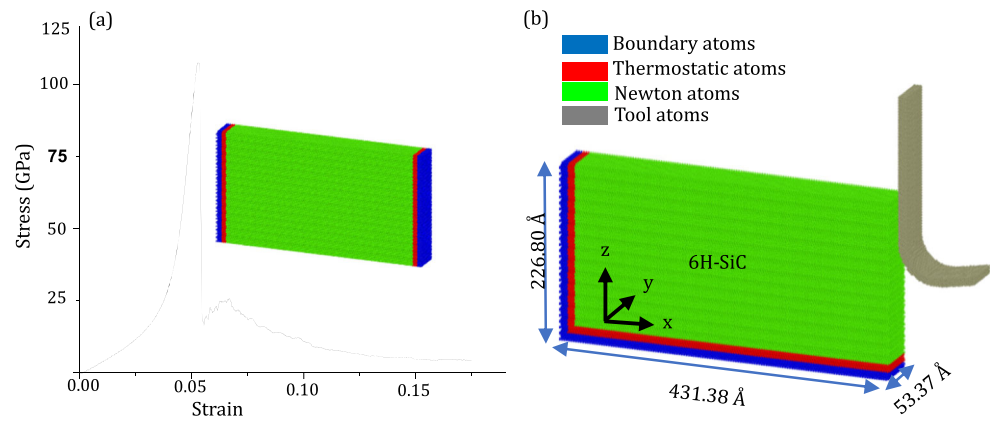

Fig. 6 Raman spectra of ductile removal surface for undeformed chip thicknesses of 50, 60, and 70 nm and unmachined surface

Fig. 7 a Molecular dynamics model for uniaxial compression and stress-strain curves from MD simulations, and **b** the nanocutting MD simulation model

2 Experimental details

As shown in Fig. 1a, the nanocutting experiments of 6H-SiC were carried out with a cutting setup under high-vacuum condition in a SEM/FIB (focused ion beam) dual beams system. The experimental setup was designed by Fang et al. [33, 34]. The setup can be used to realize a displacement of 7 μm, with a closed-loop controlled resolution of 0.6 nm in both cutting and depth directions. Online observation of the nanocutting process can be realized with the help of SEM. A single crystal diamond cutting tool with a straight cutting edge and 66-nm cutting edge radius was shaped by FIB technique to perform the experiments, as shown in Fig. 1 b.

The sample used in this study was an n-type single crystal 6H-SiC from Xiamen Powerway Advanced Material Company with a thickness of 330 μm and a size of 5 mm × 5 mm. In order to facilitate the online observation of the nanocutting process, a cutting speed of 58.79 nm/s was adopted and 1.4 mm/s for ion implant-assisted nanocutting experiments. The cutting orientation was C-face (0001) < 1–100 > of single crystal 6H-SiC.

The machined surface was investigated by EBSD and Raman spectroscopy. Phase transformation analysis was carried out by using Oxford Instruments EBSD system

(AztecHKL) with a step of 0.1 μm. The Raman spectroscopy was performed by HORIBA Scientific (XPLORA PLUS) with 638 nm laser wavelength.

3 Results and discussions

### 3.1 Morphology of the machined surface and chip by online SEM observation

Figures 2 a, b, c , d, e, and f show the nanocutting results of single crystal 6H-SiC for different undeformed chip thicknesses. With the undeformed chip thickness ≤ 70 nm, a smooth surface is obtained, which indicates that the material is removed in "ductile regime." As shown in Fig. 2 d and e, when the undeformed chip thickness is 80~90 nm, pits appear in the machined surface, although plastic deformation is still dominant. When the undeformed chip thickness increases to 100 nm (Fig. 2f), fractures take place on the machined surface.

Figures 3 a, b, c, d, e, and f show the cutting chip morphology for different undeformed chip thicknesses. With the undeformed chip thickness ≤ 70 nm, a continuous ribbon-like chip, similar to metal cutting, is formed. For the undeformed chip thicknesses of 80 nm and 90 nm (Fig. 3d, e), the chips are still continuous ribbon-like, whereas brittle fracture already occurs, which are consistent with Fig. 2 d and e. Brittle chips with irregular shape and sharp ends shown in Fig. 3 f indicate that brittle fracture is predominant in removal process.

3.2 Phase identification and dislocation analysis

The major objective for the characterization of nanocutting results is to investigate structural transformations and dislocation activities on the ductile removal machined surface.

Table 1 Detailed parameters adopted in MD simulation

Parameters	Type or values
Workpiece material	Single crystal 6H-SiC
Workpiece dimensions (x, y, z)	431.38 × 53.37 × 226.80 Å
Cutting planes and cutting direction	(0001) [−12–10]
Tool rake and clearance angles	0 °and 10°
Tool edge radius	5 nm
Depth of cut	10 nm
Cutting speed	50 m/s
Workpiece temperature	293 K

Fig. 8 Snapshots from the different nanometric cutting simulations. The upper right corner is the hydrostatic pressure distribution at the corresponding time. **a** Normal nanocutting with 10 nm depth of cut. **b** Stress-assisted nanocutting with 10 nm depth of cut under a 5.8 GPa uniaxial compression stress
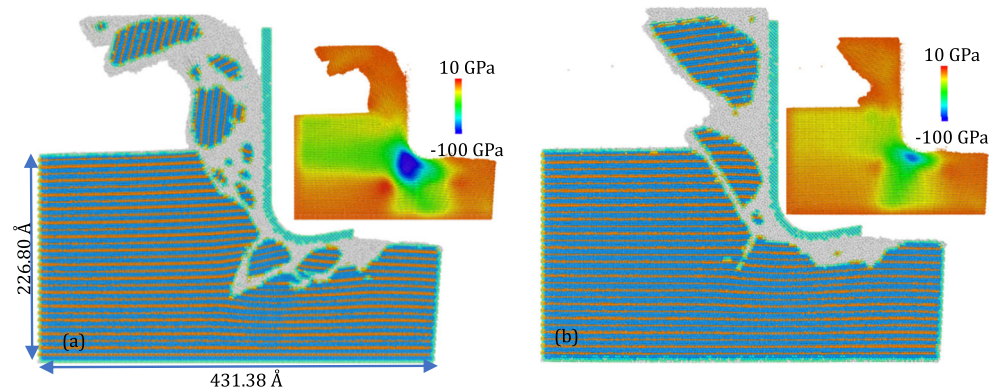
3.2.1 Phase identification

EBSD employs as an additional characterization technique to SEM and enables the identification of grain orientations and their phases on the surfaces of bulk crystals. Figure 4 shows EBSD results on phase identification and distribution of single crystal 6H-SiC after nanocutting with different undeformed chip thicknesses. The size of characterized region is 2.5 μm × 5 μm. Some other SiC polytypes (i.e., 4H, 15R, etc.) also appear in the virgin substrate area, indicated with different colors.

Significant differences can be observed from the phase identification and distribution for the machined and unmachined regions with different undeformed chip thicknesses. EBSD characterizations were conducted with two beam energies of 15 keV and 20 keV. For 15 keV beam energy, when the undeformed chip thickness was larger than 50 nm, the machined surface showed a drastic reduction of SiC crystal structures from the EBSD results. When the undeformed chip thickness was further increased to 90 nm, no backscatter Kikuchi patterns in the machined region was observed, as shown in Fig. 4 c. However, for 20 keV beam energy, SiC crystal structures can still be detected after nanocutting with the unde-

formed chip thickness of 80–100 nm, as shown in Fig. 4 d, e, and f.

The proportion of SiC crystal structure over the machining area with different depths of cut is analyzed based on the EBSD (20 kV, 2.4 nA) data, as shown in Fig. 5 a. With the increase of depth of cut up to 90 nm, the 6H-SiC structure decreases steadily, while the 15R SiC crystal structure and the areas without Kikuchi pattern increase. It shows that part of 6H-SiC structure transforms to 15R SiC crystal structure and amorphous phase [35]. When the depth of cut increased to 100 nm, the proportion of none Kikuchi pattern increased to 66%.

Figure 5 b showed the backscatter electron penetration depths in SiC for EBSD with energies of 15 keV and 20 keV calculated by Casino simulation. TEM result showed that the subsurface amorphous layer thickness of machined 6H-SiC with 90 nm depth of cut is ~23 nm (see Fig. 5c. As for 15 keV, more than 85% of the backscattered electrons originate from depth less than 23 nm; phase transformations underneath the amorphous layer cannot be detected for this energy.

3.2.2 Dislocation mobility analysis

Raman spectroscopy is an effective method for the characterization of SiC polytypes [36]. Nakashima et al. [37]

Fig. 9 Output of the DXA algorithm showing dislocation lines during nanometric cutting of 6H-SiC under **a** normal nanocutting and **b** stress-assisted nanocutting. Green line, yellow line, and red line represent dislocations with Burgers vector 1/3 < 1–210 > and 1/3 < 1–100 > and unidentified dislocations, respectively
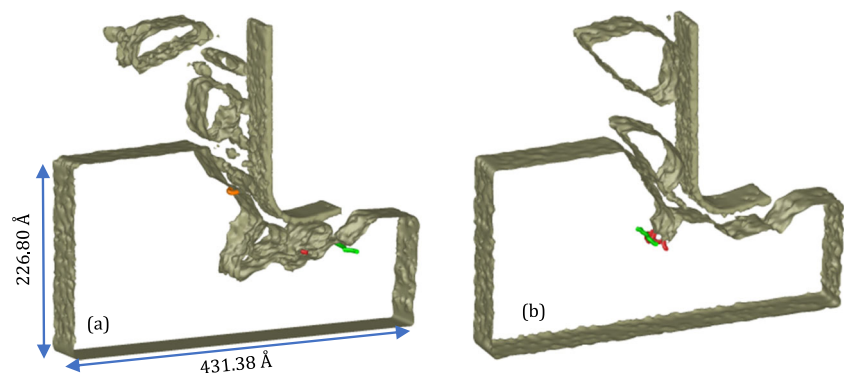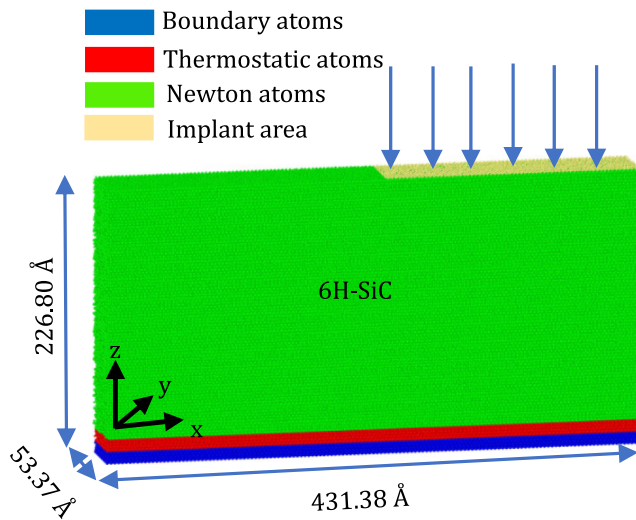
Fig. 10 The implantation MD simulation model

proved that a striking Raman band at 796 cm-1 FTO(0) (folded transverse optical) is a monitor of stacking faults for 6H-SiC.

Figure 6 shows typical Raman spectra for the nanomachined 6H-SiC regions with different undeformed chip thicknesses. As shown by the black line in Fig. 6, the FTO(0) Raman band in the unmachined surface indicates the existence of stacking faults in the original 6H-SiC substrate. Comparing with the unmachined region, the intensity of the FTO(6/6), FTO(2/6), and FTO(0), in which the numbers in parentheses represent wave vectors, Raman band in the ductile removal region decreases with the increase of undeformed chip thickness, which would be mainly caused by the subsurface damage layer [38]. In particular, the intensity of FTO(0) Raman band does not increase, which reveals that the stacking faults density does not increase for the nano-machined surface after the ductile removal process.

Table 2   Detailed parameters adopted in MD simulation

Parameters	Type or values
Workpiece material	Single crystal 6H-SiC
Workpiece dimensions (x, y, z)	$431.38 \times 53.37 \times 226.80$ Å
Implant area	20 nm × 5 nm
Number of Si ions	65
Ion doses	6.5×10^{13} ions/cm^2
Ion energy	3 KeV
Bulk temperature	293 K
Timestep	Adaptive timestep
Potential	SiC.tersoff.zbl

For single crystal 6H-SiC, the slip system (0001) < 11– 20 > is active at about 1173 K [39], and the plastic deformation occurs in 6H-SiC by dislocation movement at above 1273 K [40]. Since the nanocutting experiments in this paper were carried out with much small cutting speed of 58.79 nm/s, the maximum temperature in the cutting zone would be not sufficient to activate the slip system of 6H-SiC, and the dislocation movement was limited for the experiments here.

3.3 Methods to improve the 6H-SiC ductile machining ability

To improve 6H-SiC ductile machining ability, methods of stress-assisted and ion implant-assisted nanocutting are studied here.

#### 3.3.1 Stress-assisted nanocutting

The large-scale atomic/molecular massively parallel simulator code [41] is used to simulate nanometric cutting of 6H-SiC. The analytical bond order potential (ABOP) [42] is used to describe the interactions between Si-Si, Si-C, and C-C in the tool and workpiece and between them. Figure 7 b shows the MD model for nanometric cutting of 6H-SiC. The diamond tool is regarded as a rigid body. Periodic boundary condition is applied along the y direction. In the model of stress-assisted nanocutting, a uniaxial compression with stress of 5.8 GPa within the elastic region is applied to the 6H-SiC sample along -x-axis as shown in Fig. 7 a. Detailed nanometric cutting parameters are given in Table 1.

Figure 8 shows the subsurface damage results under normal nanocutting and stress-assisted nanocutting at 10 nm cutting depth. Results show that stress-assisted nanocutting can effectively decrease the subsurface damage under the same depth of cut.

Hydrostatic stress is associated with a change of volume leading to classical thermodynamic phase transition [43, 44]. Experimental study has revealed that the rock salt structural transformation in 6H-SiC requires a transformation pressure of 100 GPa [45]. As shown in Fig. 8, for normal nanocutting, high hydrostatic stress occurred in front of the tool cutting edge, and the maximum hydrostatic stress can reach 100 GPa, which is enough to induce the HPPT in nanometric cutting 6H-SiC. Comparing with the results of normal nanocutting, the hydrostatic stress decreases greatly in stress-assisted nanocutting, which would inhibit the HPPT occurrence.

Figure 9 shows the simulation results obtained by post-processing of the MD trajectories by using the dislocation

Fig. 11 Damage distribution after ion implantation
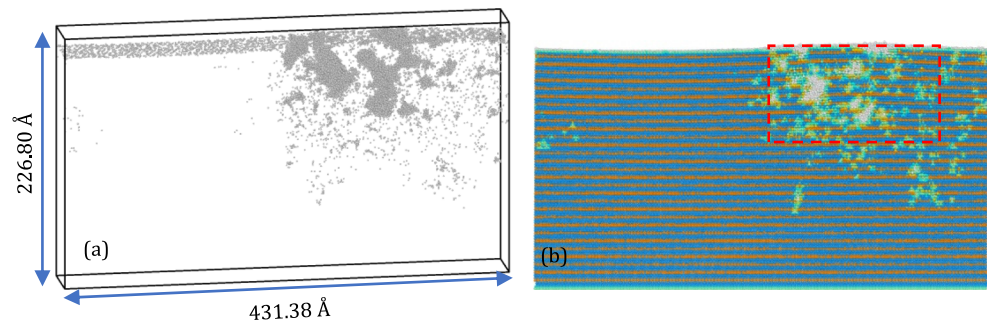
extraction algorithm (DXA). For normal machining perfect dislocations with Burgers vector 1/3 < 1–210>, some partial dislocations with Burgers vector 1/3 < 1–100 > and unidentified dislocations mainly exist in chip formation zone and the machined subsurface. However, for stress-assisted nanocutting, most of the dislocations are located in front of the tool cutting edge, as shown in Fig. 9 b. Moreover, the number of dislocations is increased in comparison with normal nanocutting.

MD simulation results show that stress-assisted method can effectively decrease the hydrostatic stress and help to activate dislocation motion, resulting in the improvement of ductile machining for stress-assisted nanocutting.

3.3.2 Ion implant-assisted nanocutting

Following the ion implant-assisted nanomachining of brittle materials proposed by Fang [31]. In this paper, ion implant-assisted nanocutting by Si ions implantation was studied by MD simulation. Figure 10 shows the MD model for ion implantation. SiC.tersoff.zbl potential [46] is used to describe the interactions between Si-Si, Si-C,

and C-C. Periodic boundary condition is applied along the x and y direction. Considering the simulation speed and simulation accuracy, the simulation method with adaptive timestep is used in the simulation. The timestep is increased from 0.001 to 1 fs during the simulation to ensure that the largest movement distance of all particles in the system is less than 0.02 Å during the single integration process [47]. Detailed nanometric cutting parameters are given in Table 2.

After implantation of 65 silicon ions into silicon carbide, structure of the substrate was analyzed, as shown in Fig. 11. Figure 11 a shows only the distribution of damaged atoms, and the atoms of normal structure are hidden. It can be seen that some areas have formed a continuous uniform damage structure. In order to quantitatively analyze the damage, the number of damaged atoms at different ion doses is counted, as shown in Fig. 12. With the increase of the number of ion implantation, the number of damaged atoms increases gradually. When the number of ion implantation reaches 65, the number of damaged atoms has exceeded 12,000. Radial distribution function of the material in the red rectangular area shown in
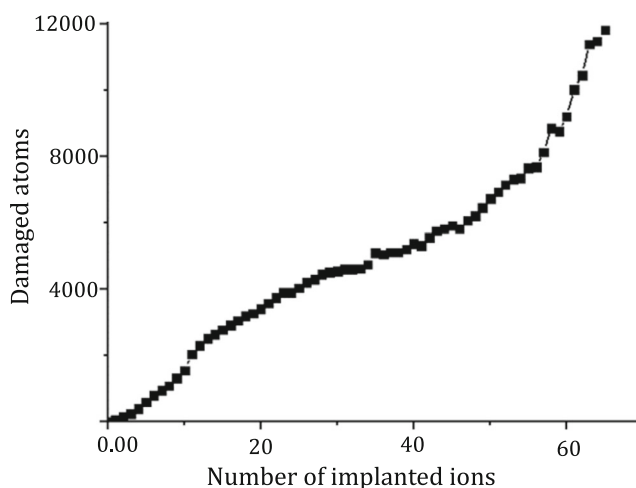

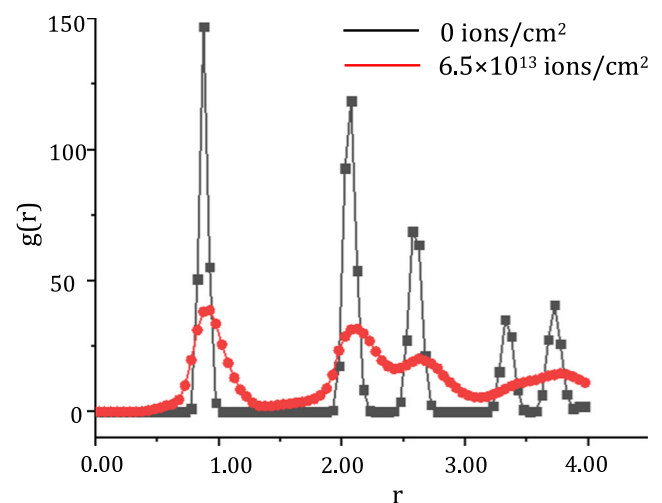Fig. 12 Curve of damage atom with ion implantation

Fig. 13 RDF of the subsurface after ion implantation

Fig. 14 Snapshots from the nanometric cutting simulations with 10 nm depth of cut by **a** normal nanocutting and **b** ion implant-assisted nanocutting. The upper right corner is the hydrostatic pressure distribution at the corresponding time
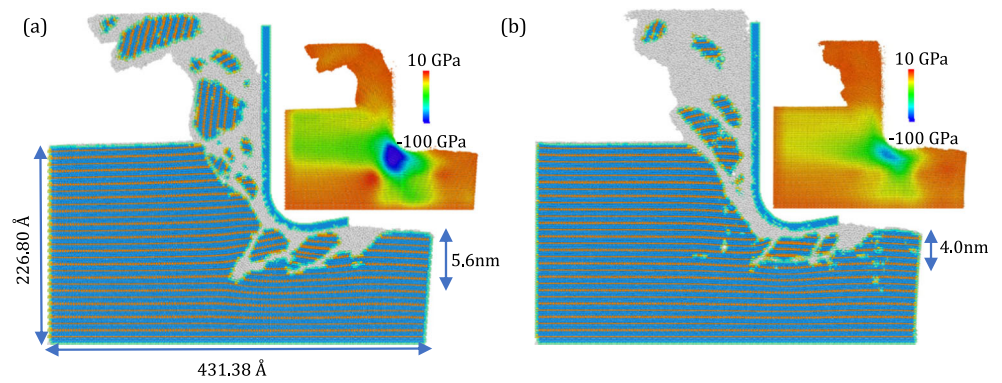
Fig. 11 b is analyzed. It can be found that the peaks are weakened and broadened after the implantation, as shown in Fig. 13. The regularity of periodic distribution was severely damaged, and the amorphous characteristics of short-range ordered and long-range disordered were reflected.

The ion implant 6H-SiC substrate was further studied the nanocutting performance comparing with normal nanocutting. Figure 14 shows the nanometric cutting simulations by normal nanocutting and ion implant-assisted nanocutting. Figure 15 shows the curve of damage layer depth with time during the normal nanocutting process. The depth of damage layer increases with the progress of cutting. Amorphous phase transition of atoms occurs in front and bottom of the tool [48], and some of the damaged atoms extend to the depth, which constitutes the subsurface
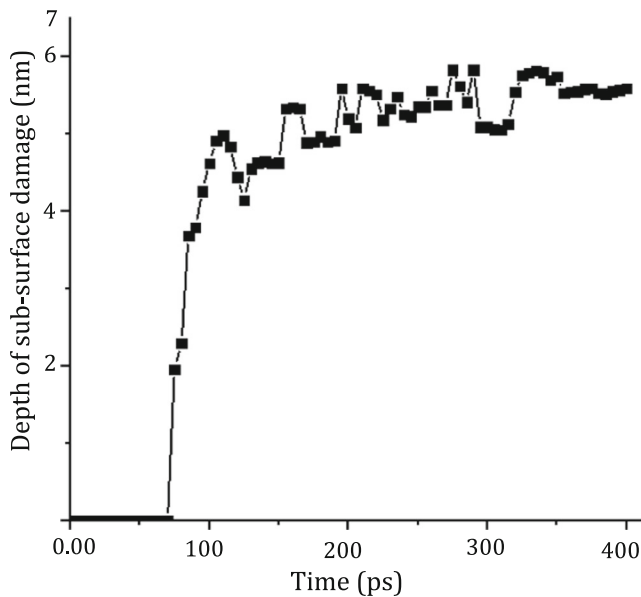
damage. As the cutting process reaches a stable state, the depth of damage layer tends to be stable gradually. Distribution of the damaged atom in the direction of subsurface damage depth both for normal nanocutting and ion implant-assisted nanocutting are shown in Fig. 16. It can be seen that the depth of subsurface damage is smaller under ion implant-assisted nanocutting, indicating that the quality of the finished surface (indicated by the deformed layer depth) appears to be better obtained under ion implant-assisted nanocutting. This can also be seen from the subsurface damage results shown in Fig. 14. As previously analyzed, ion implantation induces amorphization in the implanted region, so material removal is easier, and subsurface damage is less during the nanocutting process. Moreover, the proportion of amorphous atoms in chips increases significantly, which indicates that more materials can be removed by plastic flow, as shown in Fig. 14. By analyzing the hydrostatic stress at the corresponding time,
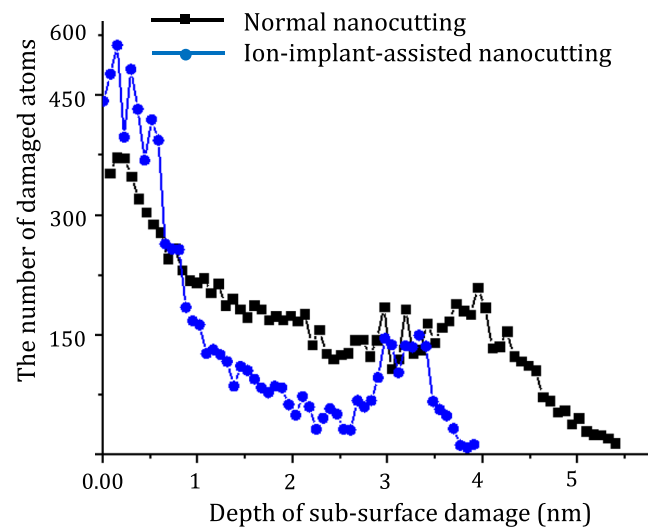

Fig. 15 Curve of subsurface damage depth with time under normal nanocutting

Fig. 16 Distribution of damaged atoms in the direction of subsurface damage depth
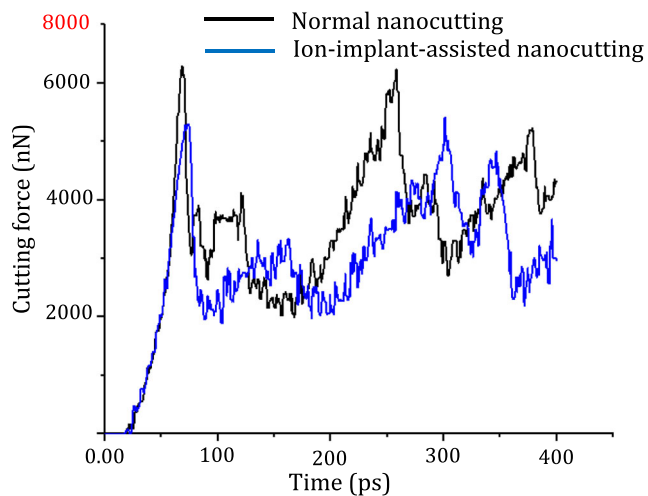
Fig. 17 Cutting force during nanometric cutting of 6H-SiC

it can be found that comparing with the results of normal nanocutting, the hydrostatic stress decreases greatly in ion implant-assisted nanocutting, which means that the material can be easily removed. This can also be seen from the cutting force variation curve shown in Fig. 17. Due to the amorphization of implanted region induced by ion implantation, the cutting force of ion implant-assisted method is significantly smaller than that under normal nanocutting. After calculation, the average cutting force under ion implant-assisted nanocutting and normal nanocutting is 2870.5 nN and 3312.8 nN, respectively, where the average cutting force decreases by 15.4%.

MD simulation results show that ion implant-assisted method can effectively increase the degree of amorphization in the ion-modified region, resulting in the improvement of ductile machining for ion implant-assisted nanocutting.

Finally, ion implant-assisted nanocutting experiments were performed to verify the MD simulation results. The Gallium ions are locally implanted into the 6H-SiC surface with 30 keV and 5×10^{16} $1/cm^2$ ion dose in our study, as indicated in Fig. 18. By using Stopping and Range of Ions in Matter

(SRIM) simulation [38], the thickness of ion implantation-induced amorphous layer has been estimated to amount to ~42 nm. With the cutting depth 90 nm each time, continuous nanocutting experiments are performed over the ion-implanted and virgin areas. After the first nanocutting, the machined surface keeps smooth in the implanted area, while brittle crack can be found in the non-implanted area, which reveals that the ion implantation enhances the machinability of the single crystal 6H-SiC, as shown in Fig. 18 a. After a further 90 nm depth nanocutting, there is still no brittle crack in the implanted area, as shown in Fig. 18 b. Although the ion implant modification layer has been removed, the stable amorphous damage layer induced by the previous nanocutting would enhance the ductile machinability for this area. For the third 90 nm depth nanocutting, the machined surfaces of both implanted and non-implanted area become brittle fractured. It shows that ion implant-assisted nanocutting can also increase ductile machining ability of 6H-SiC.

4 Conclusions

Nanocutting experiments under SEM online observation were conducted to study the removal mechanisms of 6H-SiC. The phase transformation, subsurface damage layer thickness, and stacking fault density for the machined area were studied by EBSD, TEM, and Raman characterizations. Characterization results show that part of 6H-SiC structure transforms to 15R-SiC crystal structure and amorphous phase after nanocutting. The subsurface amorphous layer thickness of machined 6H-SiC with 90 nm undeformed chip thicknesses is ~ 23 nm. Results show that stress-assisted method can effectively decrease the hydrostatic stress and help to activate dislocation motion located ahead of the tool cutting edge and ductile machining. MD simulation and continuous nanocutting experiments showed that ion implant-induced damages are helpful to improve 6H-SiC ductile machining ability.
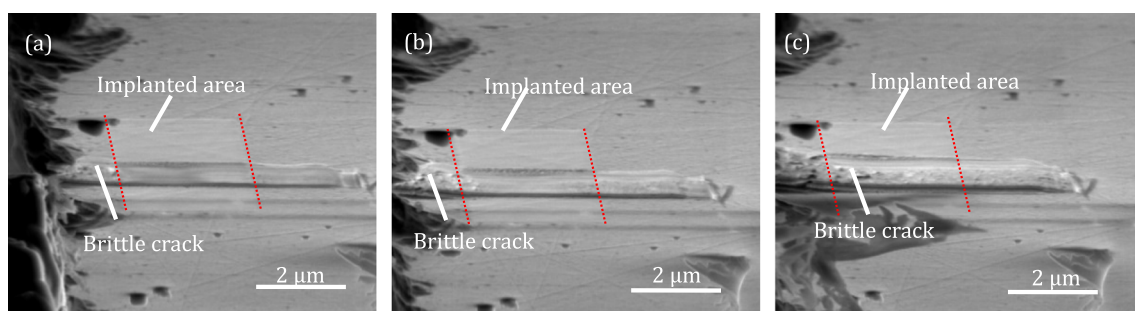

Fig. 18 The ion-implant-assisted 6H-SiC nanocutting results for continuous three times 90 nm depth of cut: **a** the first time, **b** the second time, **c** and the third time. The red dot lines show the boundary for ion implant area along the cutting direction

References

1. Khuat V, Ma Y, Si J, Chen T, Chen F, Hou X (2014) Fabrication of through holes in silicon carbide using femtosecond laser irradiation and acid etching. Appl Surf Sci 289:529–532

2. Zhang Z, Cui J, Wang B, Jiang H, Chen G, Yu J (2018) In situ TEM observation of rebonding on fractured silicon carbide. Nanoscale 10:6261–6769

3. Cui J, Zhang Z, Jiang H, Jiang H, Zou L, Guo X, Yao L, Ivan PP, Guo D (2019b) Ultrahigh recovery of fracture strength on mismatched fractured amorphous surfaces of silicon carbide. ACS Nano 13:7483–7492

4. Mélinon P, Masenelli B, Tournus F, Perez A (2007) Playing with carbon and silicon at the nanoscale. Nat Mater 6:479–490

5. Guo X, Li Q, Liu T, Kang R, Jin Z, Guo D (2017) Advances in molecular dynamics simulation of ultra-precision machining of hard and brittle materials. Front Mech Eng 12:89–98

6. Eker S, Durandurdu M (2009) Pressure-induced phase transformation of 4H-SiC: an ab initio constant-pressure study. Europhys Lett 87:36001

7. Loan PRV (1967) A study of polytypism in silicon carbide. The American Mineralogist 52:946–956

8. Fang FZ, Venkatesh V C (1998) Diamond cutting of silicon with nanometric finish. CIRP Annals-Manufacturing Technology 47:45–49

9. Fang F. Z., Wu H., Zhou W., Hu X. T (2007) A study on mechanism of nano-cutting single crystal silicon. J Mater Process Technol 184:407–410

10. Lai M, Zhang X, Fang F, Wang Y, Feng M (2013) Study on nanometric cutting of germanium by molecular dynamics simulation. Nanoscale Res Lett 8:13

11. Fang F, Xu F, Lai M (2015) Size effect in material removal by cutting at nano scale. Int J Adv Manuf Technol 80:591–598

12. Li Z, Zhang X (2017) Subsurface deformation of germanium in ultra-precision cutting: characterization of micro-Raman spectroscopy. Int J Adv Manuf Technol 91(1–4):213–225

13. Zhang ZY, Huo YX, Guo DM (2013) A model for nanogrinding based on direct evidence of ground chips of silicon wafers. Science China-Technological Sciences 56(9):2099–2108

14. Zhang Z, Song Y, Xu C, Guo D (2012) A novel model for undeformed nanometer chips of soft-brittle HgCdTe films induced by ultrafine diamond grits. Scr Mater 67(2):197–200

15. Zhang Z, Huo F, Zhang X, Guo D (2012) Fabrication and size prediction of crystalline nanoparticles of silicon induced by nanogrinding with ultrafine diamond grits. Scr Mater 67(7–8):657–660

16. Zhang Z, Wang B, Kang R, Zhang B, Guo D (2015) Changes in surface layer of silicon wafers from diamond scratching. CIRP Ann 64:349–352

17. Zhang Z, Guo D, Wang B, Kang R, Zhang B (2015) A novel approach of high speed scratching on silicon wafers at nanoscale depths of cut. Sci Rep 5:16395

18. Wang B, Zhang Z, Chang K, Cui J, Rosenkranz A, Yu J, Guo D (2018) New deformation-induced nanostructure in silicon. Nano Lett 18:4611–4617

19. Zhang Z, Du Y, Wang B, Wang Z, Kang R, Guo D (2017) Nanoscale wear layers on silicon wafers induced by mechanical chemical grinding. Tribol Lett 65:132

20. Zhang Z, Cui J, Wang B, Wang Z, Kang R, Guo D (2017) A novel approach of mechanical chemical grinding. J Alloys Compd 72:6514–6524

21. Patten J, Gao W, Yasuto K (2005) Ductile regime nanomachining of single-crystal silicon carbide. J Manuf Sci Eng 127:522–532

22. Wu ZH, Liu WD, Zhang LC (2017) Revealing the deformation mechanisms of 6H-silicon carbide under nano-cutting. Comput Mater Sci 137:282–288

23. Meng BB, Zhang Y, Zhang FH (2016) Material removal mechanism of 6H-SiC studied by nanoscratching with Berkovich indenter. Applied Physics A 122:247

24. Zhang F, Meng B, Geng Y, Zhang Y (2016) Study on the machined depth when nanoscratching on 6H-SiC using Berkovich indenter: Modelling and experimental study. Appl Surf Sci 368:449–455

25. Li Z, Zhang F, Luo X (2018) Subsurface damages beneath fracture pits of reaction-bonded silicon carbide after ultra-precision grinding. Appl Surf Sci 448:341–350

26. Goel S, Luo XC, Comley P, Reuben RL, Cox A (2013) Brittle-ductile transition during diamond turning of single crystal silicon carbide. Int J Mach Tool Manu 65:15–21

27. Xiao GB, To S, Zhang GQ (2015) The mechanism of ductile deformation in ductile regime machining of 6H SiC. Comput Mater Sci 98:178–188

28. Xiao G, To, S, Zhang G (2015) A study of chip formation in ductile-regime machining of 6H silicon carbide by molecular dynamics. International Journal of Nanomanufacturing 11:64–77

29. Goel, S., Luo, X., Reuben, R. L., & Rashid, W. B (2011) Atomistic aspects of ductile responses of cubic silicon carbide during nanometric cutting. Nanoscale Res Lett 6:589

30. Gao B, Zhai W, Zhai Q, Zhang M (2019) Novel polystyrene/CeO2-TiO2 multicomponent core/shell abrasives for high-efficiency and high-quality photocatalytic-assisted chemical mechanical polishing of reaction-bonded silicon carbide. Appl Surf Sci 484:534–541

31. Fang FZ, Chen YH, Zhang XD, Hu XT, Zhang GX (2011) Nanometric cutting of single crystal silicon surfaces modified by ion implantation. CIRP Annals-Manufacturing Technology 60:527–530

32. Zhou Z, Guo D (1987) Pre-stressed machining: combined use of heuristics and optimization methods. Proceedings of IX the ICPR 11:257–262

33. Fang FZ, Liu B, Xu ZW (2015) Nanometric cutting in a scanning electron microscope. Precis Eng 41:145–152

34. Bing L, Fengzhou F, Rui L, Zongwei X, Yanshu L (2018) Experimental study on size effect of tool edge and subsurface damage of single crystal silicon in nano-cutting. Int J Adv Manuf Technol 98:1093–1101

35. Tupitsyn EY, Arulchakkaravarthi A, Drachev RV, Sudarshan TS (2007) Controllable 6h-sic to 4h-sic polytype transformation during pvt growth. J Cryst Growth 299:70–76

36. Nakashima S, Harima H (2004) Characterization of defects in SiC crystals by Raman scattering. Springer Berlin Heidelberg 585–605

37. Nakashima S, Nakatake Y, Harima H, Katsuno M (2000) Detection of stacking faults in 6H-SiC by Raman scattering. Applied Physics Letter 77:3612–3614

38. Xu ZW, He ZD, Song Y, Xiu F, Mathias R, Xichun L (2018) Topic review: application of Raman spectroscopy characterization in micro/nano-machining. Micromachines 9:361

39. Niihara K (1979) Slip systems and plastic deformation of silicon carbide single crystals at high temperatures. Journal of the Less Common Metals 65:155–166

40. Fujita S, Maeda K, Hyodo S (2016) Dislocation glide motion in 6H SiC single crystals subjected to high-temperature deformation. Philosophical Magazine A 55:203–215

41. Plimpton S (1995) Fast parallel algorithms for short-range molecular dynamics. J Comput Phys 117:1–19

42. Erhart P, Albe K (2005) Analytical potential for atomistic simulations of silicon, carbon, and silicon carbide. Phys Rev B 71:035211

43. Goel S, Stukowski A, Luo X, Agrawal A, Reuben R (2013) Anisotropy of single-crystal 3C-SiC during nanometric cutting. Model Simul Mater Sci Eng 21:065004

44. Fang FZ, Xu F (2018) Recent advances in micro/nano-cutting: effect of tool edge. Nanomanufacturing and Metrology 1:4–31

45. Yoshida M, Akifumi O, Masaki U, Kenichi T, Osamu S (1993) Pressure-induced phase transition in SiC. Phys Rev B 48:10587

46. Devanathan R, Rubia TDDL, Weber WJ (1998) Displacement threshold energies in β-SiC. J Nucl Mater 253:47–52

47. Fu X, Xu ZW, He ZD, Hartmaier A, Fang FZ (2018) Molecular dynamics simulation of silicon ion implantation into diamond and subsequent annealing. Nuclear Instruments & Methods in Physics Research In press

48. Xie W, Fang F (2019) Cutting-based single atomic layer removal mechanism of monocrystalline copper: atomic sizing effect. Int J Adv Manuf Technol 1:12